nature physics

ARTICLES

PUBLISHED ONLINE: 11 APRIL 2016 | DOI: 10.1038/NPHYS3720

Inertially confined fusion plasmas dominated by alpha-particle self-heating

O. A. Hurricane[1]*, D. A. Callahan[1], D. T. Casey[1], E. L. Dewald[1], T. R. Dittrich[1], T. Döppner[1], S. Haan[1], D. E. Hinkel[1], L. F. Berzak Hopkins[1], O. Jones[1], A. L. Kritcher[1], S. Le Pape[1], T. Ma[1], A. G. MacPhee[1], J. L. Milovich[1], J. Moody[1], A. Pak[1], H.-S. Park[1], P. K. Patel[1], J. E. Ralph[1], H. F. Robey[1], J. S. Ross[1], J. D. Salmonson[1], B. K. Spears[1], P. T. Springer[1], R. Tommasini[1], F. Albert[1], L. R. Benedetti[1], R. Bionta[1], E. Bond[1], D. K. Bradley[1], J. Caggiano[1], P. M. Celliers[1], C. Cerjan[1], J. A. Church[1], R. Dylla-Spears[1], D. Edgell[2], M. J. Edwards[1], D. Fittinghoff[1], M. A. Barrios Garcia[1], A. Hamza[1], R. Hatarik[1], H. Herrmann[3], M. Hohenberger[2], D. Hoover[4], J. L. Kline[3], G. Kyrala[3], B. Kozioziemski[1], G. Grim[1], J. E. Field[1], J. Frenje[5], N. Izumi[1], M. Gatu Johnson[5], S. F. Khan[1], J. Knauer[2], T. Kohut[1], O. Landen[1], F. Merrill[3], P. Michel[1], A. Moore[1], S. R. Nagel[1], A. Nikroo[4], T. Parham[1], R. R. Rygg[1], D. Sayre[1], M. Schneider[1], D. Shaughnessy[1], D. Strozzi[1], R. P. J. Town[1], D. Turnbull[1], P. Volegov[3], A. Wan[1], K. Widmann[1], C. Wilde[3] and C. Yeamans[1]

Alpha-particle self-heating, the process of deuterium–tritium fusion reaction products depositing their kinetic energy locally within a fusion reaction region and thus increasing the temperature in the reacting region, is essential for achieving ignition in a fusion system. Here, we report new inertial confinement fusion experiments where the alpha-particle heating of the plasma is dominant with the fusion yield produced exceeding the fusion yield from the work done on the fuel (pressure times volume change) by a factor of two or more. These experiments have achieved the highest yield (26 ± 0.5 kJ) and stagnation pressures (≈220 ± 40 Gbar) of any facility-based inertial confinement fusion experiments, although they are still short of the pressures required for ignition on the National Ignition Facility (∼300–400 Gbar). These experiments put us in a new part of parameter space that has not been extensively studied so far because it lies between the no-alpha-particle-deposition regime and ignition.

Previously, we reported on experiments on inertial confinement fusion experiments (ICF)[1] at the US National Ignition Facility (NIF)[2] where the fusion energy produced was greater than the amount of energy deposited into the fusion fuel (fuel gain > 1)[3]. Here, we discuss new results[4–6] using a simple dynamic model of the hotspot to gain insight into the data. We find that our highest performing experiments sit close to the point where energy deposition from alpha heating is nearly balanced by radiation losses through bremsstrahlung. We discuss how asymmetries in the fuel layer develop and can produce weak spots in the shell as it implodes allowing the hotspot to 'vent' and preventing us from achieving higher stagnation pressure and yield. Future experiments at the NIF will address these asymmetries to make optimum use of the energy absorbed in the implosion process.

The main purpose of an implosion is to act as a pressure amplifier—this is true whether the implosion is driven by X-rays (the case for indirect drive on the NIF), directly by lasers, or by magnetic fields. ICF implosions, by their nature, use energy inefficiently, delivering only a small fraction of the absorbed energy from the drive to a thin layer of fusion fuel (50% deuterium and 50% tritium, 'DT'), which is initially in a cryogenic state[7]. The process of creating plasmas from solid materials and X-rays is how most of the laser energy is expended. Ablation pressure drives the implosion inwards on itself, ultimately accelerating the implosion to very high speeds (∼300–400 km s^{-1}). In the process, the thin shell of DT fuel and remaining ablator material (see Fig. 1) acquires kinetic energy (∼8–15 kJ) and generates a central hotspot of lower density DT as the centre of the implosion heats.

After acquiring peak kinetic energy, a shell of DT fuel and any remaining ablator, with effective mass $\epsilon m_{\rm shell}$, velocity $v_{\rm imp} = -\dot{R} = -{\rm d}R/{\rm d}t$, and inner radius R, decelerates in time, t, according to

$$\frac{d\left(\epsilon m_{\rm shell}\dot{R}\right)}{{\rm d}t} = 4\pi R^2 P_{\rm hs} \qquad (1)$$

As the pressure in the centre of the implosion—the 'hotspot' pressure $P_{\rm hs} = 0.77\rho_{\rm hs}T_{\rm hs}$ (in gigabar, g cm^{-1}, kiloelectronvolt units)—increases, both the hotspot density, $\rho_{\rm hs}$, and thermal temperature, $T_{\rm hs}$, rise. At this point in time the NIF laser has delivered its full laser pulse and the ablation pressure external to the implosion becomes negligible in comparison with the central pressure. At the moment the deceleration of the implosion begins, a shock wave transits outward from the inner surface of the fuel to the outer surface. As the DT fuel is compressible, this effectively means the full inertia of the DT fuel and remaining ablator does not act on the hotspot, but only on the shocked fraction of the fuel, hence the

[1]Lawrence Livermore National Laboratory, Livermore, California 94551, USA. [2]Laboratory for Laser Energetics, Rochester, New York 14623, USA. [3]Los Alamos National Laboratory, Los Alamos, New Mexico 87545, USA. [4]General Atomics, La Jolla, California 92121, USA. [5]Massachusetts Institute of Technology, Cambridge, Massachusetts 02139, USA. *e-mail: hurricane1@llnl.gov

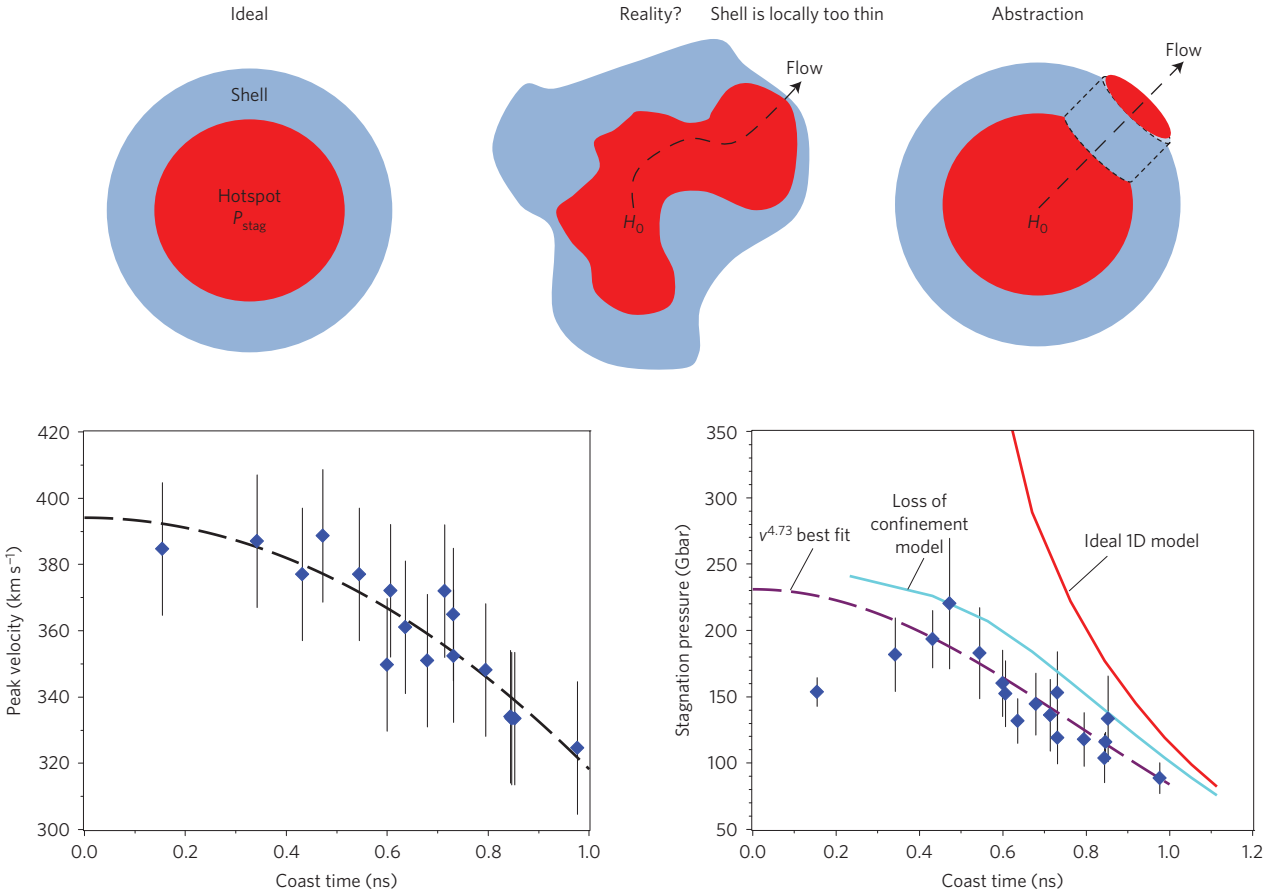

Figure 1 | Hotspot pressure versus coasting time (implosion speed). A schematic of a NIF implosion near peak-compression is round (upper left) ideally, with a dense shell (blue) of compressed DT fuel and remaining ablation material surrounding a much lower density (red) hotspot. As the 'coast time' is reduced, by extending the laser pulse, the implosion speed increases, and the hotspot pressure should rapidly increase according to ideal implosion models (lower right, red curve). The coast time (lower left) equals the implosion bang time minus the time the laser is turned off and is empirically related to implosion speed (best fit: $v_{imp} = 394.11 - 75.9t^2_{coast}$). Although implosion data from NIF do show an increase in hotspot pressure as implosion speed increases (lower right, blue data points), the rate of increase is much less than ideal. In reality, implosions may not have the ideal 1D geometry, but instead may have highly modulated 3D shell and hotspot geometries (upper middle). Thin spots of low areal density in the shell would provide little inertial confinement and would allow a path for hotspot energy and mass loss (upper right) that would not occur in the ideal implosion case. Including the effects of a lossy implosion is consistent with the NIF data (lower right; cyan curve). The model that produced the cyan curve assumes $A_{leak} \sim v^4$ (a scaling expected from Rayleigh–Taylor-like growth). The purple dashed curve is a power-law best fit to the data that shows $P_{hs} \sim v^{4.73}$. Here, the P_{stag} data are those inferred from the measured T_{ion}(DT). All error bars, 1σ.

efficiency factor, $\epsilon \leq 1$. Poor implosion symmetry (that is, time-dependent shape) or break-up of the imploding shell can also effectively lower ϵ when applying equation (1) to an implosion experiment. Generally in ICF implosions on NIF, because of the high densities and pressures achieved, inter particle collisions force the ion and electron temperatures to be approximately equal in the fusion plasma: $T_{ion} \approx T_e$, so we generally just refer to T_{hs} here. The in-falling shell of DT fuel does mechanical PdV (pressure times volume change) work on the lower density hotspot, increasing the hotspot internal energy and therefore temperature according to

$$c_{DT}\frac{dT_{hs}}{dt} = Q_\alpha - Q_{Brems} - Q_{cond} - \frac{4\pi R^2 P_{hs}\dot{R}}{m_{hs}} - \frac{(\rho_{hs}v^3_{esc} + 3P_{hs}v_{esc})A_{leak}}{2m_{hs}} \quad (2)$$

where the DT heat capacity is $c_{DT} = 0.115\,\mathrm{GJ\,g^{-1}\,keV^{-1}}$, $Q_{Brems} = 3.1 \times 10^7 \rho_{hs}\sqrt{T_{hs}}$ (GJ g^{-1} s^{-1}) is the specific cooling power of bremsstrahlung X-rays[8] in the optically thin limit (see Methods), and $Q_{cond} = 5.384 \times 10^3 T^{3.21}/(\rho^{0.806}_{hs}R^2_{hs})$ (GJ g^{-1} s^{-1}) is a modern version of the Spitzer–Harm[9] electron heat conduction model ($Q_{cond} = 5.9 \times 10^3 T^{7/2}/(\rho_{hs}R^2_{hs})$ in GJ g^{-1} s^{-1}) based on the Sesame[10] equations of state. The alpha-particle self-heating contribution to the hotspot specific power, $Q_\alpha = 8.18 \times 10^{24}\rho_{hs}f_\alpha\langle\sigma v\rangle$ (GJ g^{-1} s^{-1}), depends on the DT fusion reaction rate $\langle\sigma v\rangle \approx 2.68 \times 10^{-20} T^{3.9}_{hs}$ cm^3 s^{-1} (in the range of 3 keV $< T_{hs} <$ 5 keV relevant to the experiments discussed herein—see Methods) and the fraction, f_α, of alpha-particles stopped inside the hotspot[11] where

$$f_\alpha = 1 - \frac{1}{4[(\rho r)_{hs}/\rho\lambda_\alpha]} + \frac{1}{160[(\rho r)_{hs}/\rho\lambda_\alpha]^3} \quad (3)$$

where the alpha-particle stopping range can be found from[8]

$$\rho\lambda_\alpha = \frac{0.025T^{5/4}_e}{1 + 0.0082T^{5/4}_e} \quad (4)$$

in centimetre, gram, kiloelectronvolt units.

The last term in equation (2) represents, in our simplified picture (upper right-hand side of Fig. 1), the total kinetic plus internal

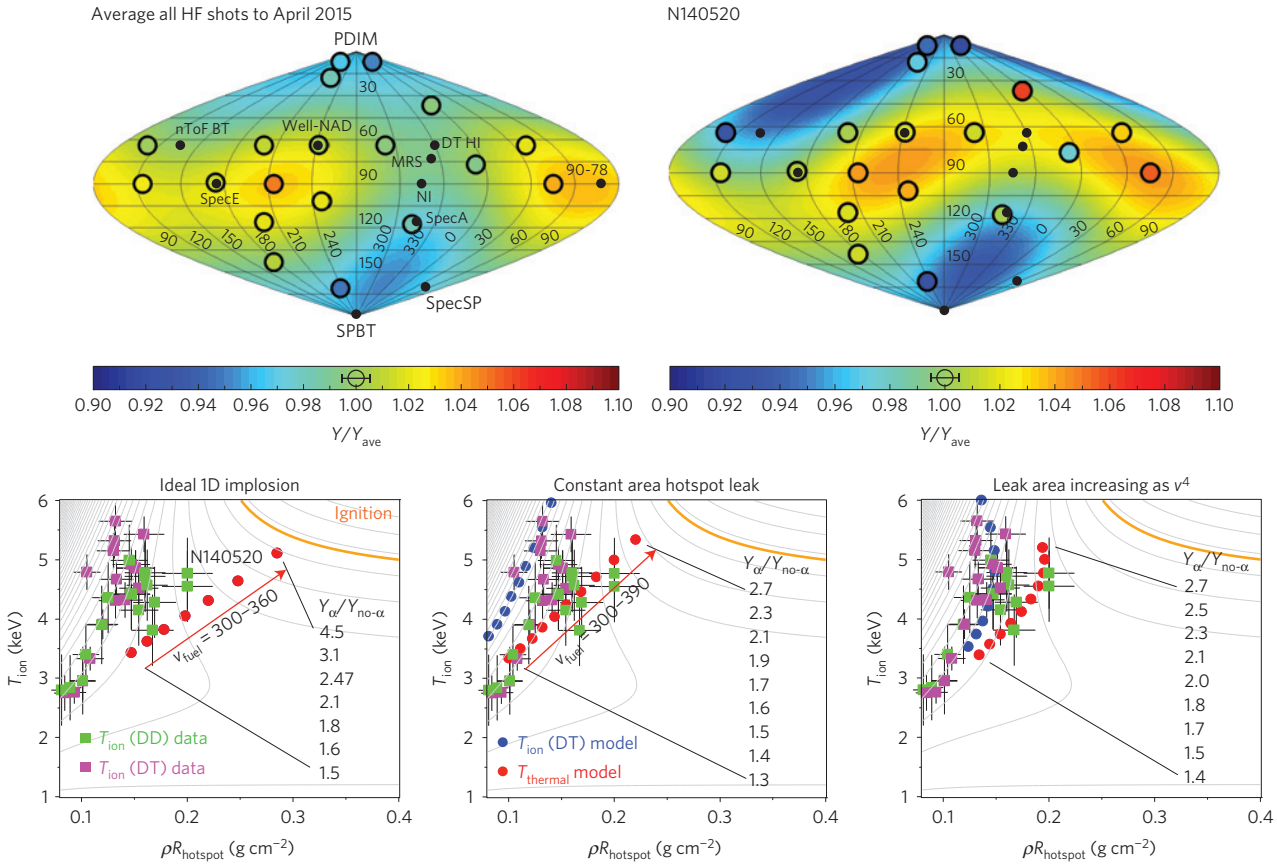

Figure 2 | 3D implosion morphology and implosion data located in a parameter space relevant to ignition. Flange activation diagnostics (FNADs), which are radiochemical detector foils arranged around the NIF chamber, reflect the areal density of material that implosion-generated neutrons pass through on the way to the detector when appropriately normalized to an isotropic neutron source[19]. The typical high-foot (HF; as well as most other) implosions on NIF do not show uniform activation levels (upper left), but instead show lower levels of activation at the poles (blue) of NIF and higher non-axisymmetric levels of activation around the waist (red)—an activation pattern that implies an implosion shell that is thick on the poles and thin, in spots, around the waist. For higher velocity and higher performance implosions, the same pattern is observed (upper right), but with a greater degree of variation. NToF-measured T_{ion} imply high-speed hydrodynamic flows in the neutron-producing regions of our implosions by the fact that different lines of sight show different temperatures and by the fact that the T_{ion}(DT) and T_{ion}(DD) differ outside the expected 300 eV level with the differences becoming more and more apparent as the implosions are driven to higher and higher velocity (bottom frames). A 1D implosion is expected to have a higher hotspot ρR for a given T_{ion} than is reflected in the data (bottom left) with $T_{thermal}$ degenerate with T_{ion}(DT). Model implosions with a shell defect (perforated shell) break the degeneracy of $T_{thermal}$ and T_{ion}(DT) and better track the actual NIF data for the suite of high-foot implosions (centre and right bottom frames with $D=10^{-4}(R_0/R)^2$ and $D=10^{-4}(R_0/R)^2(v_0/380)^4$ respectively). SPBT, south-pole bang time. All error bars, 1σ.

energy lost from the hotspot by ejecting hotspot mass through one or more weak spots or perforations (collectively of cross-sectional area A_{leak}, which defines a dimensionless 'defect', $D=A_{leak}/4\pi R^2$) in the shell. Non-uniformities in the implosion grow owing to unstable growth in convergence and create variations in shell areal density, $(\rho R)_{shell}$ (see Fig. 1) that, if extreme enough, essentially provide little to no inertial confinement of the hotspot—this is what D is meant to represent. Time-dependent asymmetries in the hohlraum-generated X-ray bath[12,13] that drive the ablation pressure of the capsule are implicated. Perforations in the shell could additionally be produced by growth of baroclinic vorticity seeded by engineering features such as capsule fill tubes (the $\sim$10 − µm-diameter glass tube that is used to fill the capsule with DT) or mounting membranes ('tents' that are diaphragms of $\sim$15–45 nm thickness plastic that hold the capsule in the centre of the hohlraum). The velocity, $v_{esc}=\sqrt{2H_{hs}/m_{hs}}$, of mass and energy outflow through a weak spot in the shell is given by the stagnation enthalpy, $H_{hs}=E_{hs}+P_{hs}V_{hs}$, at the centre of the implosion because the enthalpy outside the shell is small in proportion to the ablation pressure (hundreds of megabar) being small compared with an ICF implosions central pressure (hundreds of gigabar).

The ideal boundary between an un-ignited and ignited fusion state is given by the right-hand side of equation (2) with $\dot{R}=0$ and $A_{leak}=0$, consistent with the condition of Lawson[8,14]. That is, when in the absence of external heating, the power from alpha-particle self-heating outstrips the losses of power from radiation and electron conduction ($Q_\alpha > Q_{Brems}+Q_{cond}$) the plasma temperature rapidly increases in an explosive manner. The nearly hyperbolic boundary defined by $Q_\alpha = Q_{Brems}+Q_{cond}$ (see Fig. 2, bottom frames) depends solely on T_{hs} and the areal density of the hotspot, $(\rho R)_{hs}$ (ref. 8), so showing our implosion experiment data in the space of these two parameters is the most appropriate metric for gauging how far from ignition our results are at present (yield is not a useful metric for gauging proximity to ignition because ignition is a threshold process).

Following from equations (3)–(4) $\sim$70% of the fusion alphas are stopped in the hotspot for our implosion. The alpha-particles created during the period of DT fusion that do not stop in the hotspot are stopped in the inner surface of the much denser compressed DT fuel shell, depositing their energy there. Electrons carrying heat outward from the hotspot similarly stop in the inner surface of the DT fuel shell and also deposit their energy. The

Table 1 | Table of input and derived yield amplification metrics.

Shot	E_{laser} (MJ) absorbed	m_{abl} (μg)	m_{fuel} (μg)	$Y_\alpha/Y_{no\text{-}\alpha}$ (dm)	$Y_\alpha/Y_{no\text{-}\alpha}$
N130501	1.1±0.022	2,735	177	1.23±0.041	1.19±0.02
N130530	1.26±0.025	2,819	179	1.16±0.029	1.14±0.01
N130710	1.28±0.026	2,818	182	1.3±0.054	1.25±0.03
N130802	1.29±0.026	2,738	177	1.16±0.029	1.14±0.02
N130812	1.44±0.029	2,781	179	1.4±0.072	1.53±0.06
N130927	1.63±0.033	2,784	185	1.69±0.12	1.64±0.07
N131119	1.67±0.033	2,727	179	1.75±0.135	1.69±0.1
N131219	1.39±0.028	2,410	179	1.45±0.081	1.55±0.08
N140120	1.59±0.032	2,769	179	1.8±0.14	2.08±0.13
N140225	1.35±0.027	2,472	179	1.6±0.11	1.51±0.06
N140304	1.61±0.032	2,773	182	2.06±0.19	1.96±0.13
N140311	1.49±0.030	2,547	187	1.9±0.16	1.88±0.11
N140511	1.60±0.032	2,690	180	1.85±0.15	1.95±0.09
N140520	1.51±0.030	2,548	185	2.25±0.22	2.22±0.14
N140707	1.39±0.028	2,267	180	1.76±0.14	1.79±0.09
N140819	1.55±0.031	2,304	185	1.75±0.14	1.75±0.09

Column 2 is laser energy absorbed (incident-backscatter) by the hohlraum (typically 10–15% of this is absorbed by the imploding capsule). The ablator mass (column 3), m_{abl}, is generally reduced to 5–10% of this value at peak implosion velocity. Column 4 is the deuterium–tritium fuel mass loaded into the capsule. Column 5 shows the alpha-heating yield increase determined from the dynamic model (dm), and column 6 shows the same quantity calculated using the method of references[23,35].

deposition of energy into DT fuel causes it to ablate inwards and add DT mass to the hotspot[15,16] (and return the energy that was deposited into the fuel to the hotspot) as the hotspot heats, according to the expression

$$\mathrm{d}m_{hs}/\mathrm{d}t = \frac{m_{hs}}{0.115T}\left[Q_\alpha\left(\frac{1-f_\alpha}{f_\alpha}\right)+Q_{cond}\right]-\rho_{hs}v_{esc}A_{leak} \qquad (5)$$

where the last term represents the hotspot mass loss due to the flow of hotspot material driven out through a weak spot/perforation in the shell as the internal hotspot pressure rises (see Fig. 1). As the hotspot mass, density and temperature evolve in time, the fusion yield rate can be calculated from $\mathrm{d}Y/\mathrm{d}t = 5.0\times10^6\cdot m_{hs}Q_\alpha/f_\alpha$ in kilojoule units, where the factor of 5 comes from the fact that only 20% of the total DT fusion yield comes from alpha-particles (the other 80% coming from neutrons). Although not immediately obvious, combining equations (2) and (5), using the fact that the hotspot internal energy is $E_{int} = 0.115m_{hs}T_{hs} = 3/2P_{hs}V_{hs}$ (where $V_{hs} = 4\pi/3R_{hs}^3$ is the hotspot volume) one obtains an equation (like ref. 17) for hotspot pressure evolution,

$$\dot{P}_{hs}+5P_{hs}\frac{\dot{R}}{R} = \frac{P_{hs}}{0.115T}\left(\frac{1}{f_\alpha}Q_\alpha-Q_{Brems}-Q_{leak}\right)-P_{hs}\frac{\rho_{hs}v_{esc}A_{leak}}{m_{hs}} \qquad (6)$$

where $Q_{leak} = A_{leak}(\rho_{hs}v_{esc}^3+3P_{hs}v_{esc})/(2m_{hs})$ is the cooling of the hotspot due to energy loss through a perforation in the imploding shell with the last term in the equation being the effect of hotspot mass loss though the shell perforation. In ref. 17, the loss terms in equation (6) are not present and the fusion reaction rate is assumed to scale differently. The non-ideal effect in equation (6), a perforated implosion, is conceptually different from the non-ideal effect of Rayleigh–Taylor instability-driven spikes reducing the effective hotspot size[18]. When the right-hand side of equation (6) is negligible, adiabatic compression, $P_{hs}R^5 = \text{constant}$, is recovered (see the Methods). Note that when $Q_\alpha = f_\alpha Q_{Brems}$ in equation (6), $T = 4.3$ keV, which is the classic textbook 'ignition temperature'[8] and is a representative burn-averaged temperature of many of our high-foot implosions.

This dynamic model, equations (1)–(5), or equivalently equations (1), (2) and (6), can be constrained to implosion time-integrated data to form a picture of the dynamics around the time of peak X-ray and neutron emission ('bang time'). It also unfolds the degree of alpha-particle self-heating over the duration of the fusion burn, which is the primary purpose of the above development. When constrained to a series of high-foot experiments on the NIF where the implosion speed is increased by keeping the laser drive on longer into the implosion as measured by a reduction in the 'coast time', the time between bang time and the time the laser is shut off, the model with shell perforations seems to capture the pressure data trend (Fig. 1). The data scaling shows that $P_{stag}\sim v^{4.73}$ until a peak of ~220 Gbar, but then declines.

As seen in Fig. 2, as our implosion experiments have progressed to higher temperatures and hotspot areal densities as a result of being driven with successively higher amounts of laser energy and therefore fuel kinetic energy, the different interpretations of $(\rho R)_{hs}$ and T_{hs} differ outside of standard error bars. For these same implosions, shell areal density variations as inferred from neutron activation diagnostics[19] show more variation (for example, Fig. 2). For the most compressed implosions shell areal density variations are estimated to be as large as ~50%. Experiments driven with relatively low laser energies of 1.3–1.5 MJ occupy the region around $T_{hs}\sim3$ keV and $(\rho R)_{hs}\sim0.1\,\mathrm{g\,cm^{-2}}$, and do not show differences in temperature inference even though X-ray and neutron imaging of these experiments showed non-ideal (for example, toroidal) shape[20–22] at the time of peak X-ray and neutron brightness.

For ICF implosions neither T_{hs} nor $(\rho R)_{hs}$ is measured directly, they are instead inferred from other diagnostic data. Hotspot areal density, $(\rho R)_{hs}$, is inferred[3,23,24] from a combination of data coming from the fusion yield measurement[25,26], a temporal measurement of the fusion burn duration, imaging data from X-ray emission[27,28], imaging data from neutron emission[29,30], and the ion temperature. Burn- and volume-averaged ion temperature quantities (T_{ion}) are directly related to the temporal spread, full-width at half-maximum, of the neutron-time-of-flight (NToF) detector[31] signals using simple formulae[32]. As DT fusion neutrons, with peak energy around 14.1 MeV, travel faster and are scattered less than DD fusion neutrons, with peak energy around 2.5 MeV, the NToF detector can be used to obtain two temperature measurements of the fusion regions they sample—a T_{ion}(DT) and T_{ion}(DD). Ideally, $T_{ion}(\mathrm{DT})\approx T_{ion}(\mathrm{DD})$, which simplifies the data interpretation, but even for an ideal one-dimensional (1D) ICF implosion T_{ion}(DT) will exceed T_{ion}(DD) by ~200–300 eV owing to the electron-

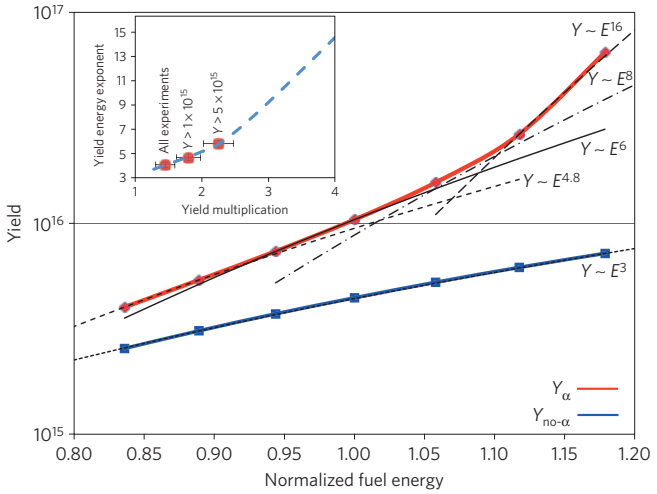

Figure 3 | The scaling of fusion yield with fuel kinetic energy. Without alpha-particle self-heating, fusion yield is expected to scale as a constant power of energy (blue curve). With alpha-particle self-heating, the fusion yield is expected to scale with an ever-increasing power of energy (red curve). High-foot implosion experiments have exhibited yield scaling with $E^{4-5.8}$ depending on which subset of the suite of data is examined[6]. All error bars, 1σ.

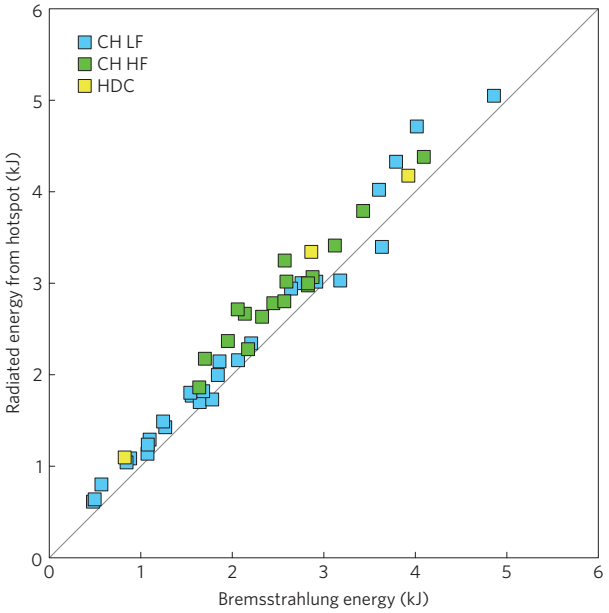

Figure 4 | X-ray energy radiated by hotspots from a variety of implosion experiments. 1D transport modelling of radiated energy from low-foot (LF) implosions[37] (blue points) that are designed to achieve high compressions, but are R–T unstable, high-foot (HF) implosions[38] (green points) that are designed to be more resistant to R–T instability, and high-density carbon (HDC) ablator experiments[39] (yellow points) is compared to the radiated energy calculated using the optically thin limit of bremsstrahlung X-rays. Perhaps fortuitously, the agreement between the detailed transport model and the simple bremsstrahlung model is quite good. CH, carbon–hydrogen (that is, plastic, ablator material).

conduction-limited radial temperature profile. In fact, $T_{ion}(\mathrm{DT})$ and $T_{ion}(\mathrm{DD})$ can also differ owing to a number of non-ideal factors such as scattering differences[33] and Doppler motion spreading of the temporal signal registered by the NToF diagnostic if the fusion region is undergoing particular vortex[34] or shearing motions. If $T_{ion}(\mathrm{DT})$ and $T_{ion}(\mathrm{DD})$ differ owing to motion in the fusion region, then mathematically we expect $T_{hs} \leq T_{ion}(\mathrm{DD}) \leq T_{ion}(\mathrm{DT})$. As can be observed in Fig. 2 (bottom frames), as implosion velocity is increased in our experiments $T_{ion}(\mathrm{DT})$ and $T_{ion}(\mathrm{DD})$ do indeed differ by as much as 1.4 keV. One interpretation of this temperature difference is that it is an indication of some probable vortical or shearing fluid motions in the fusing DT plasma, but if one simply applies the formula[34], $T_{hs} = 5T_{ion}(\mathrm{DD}) - 4T_{ion}(\mathrm{DT})$, unphysically low temperatures (that is, a contradiction) are obtained. (Some researchers would also propose kinetic effects as being responsible for the observed difference in $T_{ion}(\mathrm{DT})$ and $T_{ion}(\mathrm{DD})$, but estimation of the Knudsen number in our implosions' hotspots indicates that kinetic effects should be quite small.) It is likely that flows over some region, but not necessarily all, of the hotspot plasma in combination with scattering effects, through a broken up shell as implied by activation diagnostics[19], are the primary drivers for the observed ion temperature differences. The model that best tracks the trend of $T_{ion}(\mathrm{DT})$ and $(\rho R)_{hs}$ (Fig. 2 lower right-hand side) as well as the P_{stag} (Fig. 1) is one where $A_{leak} \sim v^4$ and the observed $T_{ion}(\mathrm{DT})$ is treated as a superposition of two distributions, a 1D implosion contribution and a flow contribution. The perforation area scaling as v^4 can be simply understood as the consequence of deceleration phase break-up: from a free-fall assumption $gd \sim v^2$ (g being the effective gravity and d being a typical inward directed Rayleigh–Taylor spike amplitude) and a weakly nonlinear assumption $d \sim \lambda$ (λ being a typical feature wavelength), one obtains $A_{leak} \sim \lambda^2 \sim v^4$. Collectively, diagnostics and models that best match the data imply a picture of NIF high convergence implosions that are consistent with an implosion shell that is highly distorted and perforated.

In spite of implosions having non-ideal shape, the degree of alpha-particle self-heating in the implosions can be determined (as seen in Fig. 2). An iterative procedure can be used to match the dynamic model to the bang-time data (Y, burn-averaged T_{ion}, and hotspot volume) and inferred burn-averaged P_{hs} and $(\rho R)_{hs}$ data to within error bars for a given experiment as is shown in Fig. 2. Measurements such as the duration of the fusion burn (that is, 'burn width', τ) is automatically matched through this procedure because the inferred data incorporate τ by construction[3]. This procedure can be used to infer the thermodynamic state of the hotspot at the time of peak fuel velocity (because this information is the initial data for the differential equations above). Moreover, equations (1)–(5), or equivalently equations (1), (2) and (6) can then be solved again forwards in time with the Q_α term dropped thereby calculating the time-dependent and burn-averaged properties of an equivalent implosion without any alpha-particle self-heating. Thus, we arrive at a method for determining the impact of alpha-particle self-heating on an individual implosion experiment on a case-by-case basis. The results can be compared (Table 1) with a correspondence between yield amplification ($Y_\alpha/Y_{no\text{-}\alpha}$) and measured yield and down-scatter ratio[26,33] (the ratio of the number of neutrons measured in the energy range from 10 to 12 MeV over the number of neutrons measured in the energy range from 13 to 15 MeV) that was arrived at by a fit to a large database of simulated implosions[23,35] as an alternative method for determining alpha-heating.

For a given ablator mass efficiency, with the thermodynamic properties of a given implosion experiment determined from the above procedure, we can then vary the amount of kinetic energy, $E_k = (1/2)\epsilon m_{shell} v_{imp}^2$ in the dynamic model to obtain the scaling of fusion yield with and without alpha-particle self-heating (Fig. 3). As can be seen in Fig. 3, as the fusion fuel acquires higher levels of energy, the fusion yield responds to the fuel energy with an ever-increasing exponent, $Y \sim E_k^A$, where $A \geq 3$, with $A = 3$ being the case of zero alpha-particle self-heating (for example, ref. 36). For $A > 5.1$, the yield multiplication due to alpha-particle self-heating doubles. This scaling of fusion yield with energy (or equivalently implosion velocity) allows us to determine the degree of alpha-particle self-heating for a suite of implosion experiments as an alternative method to the case-by-case determination. It has

been observed[6] that the fusion yield scales with delivered laser energy, E_{laser}, as $Y \sim E_{laser}^4$ for the suite of high-foot experiments, shots N130501–N140819 (where on the NIF each 'shot' is labelled in year–month–day format YYMMDD). Excluding shots whose fusion yields are below 1×10^{15} neutrons from the data set, a scaling of $Y \sim E_{laser}^{4.7}$ is found. Furthermore, excluding all shots whose fusion yields are below 5×10^{15} neutrons from the data set, a scaling of $Y \sim E_{laser}^{5.8}$ is found. It is expected that E_k is related to E_{laser} through a series of efficiency factors, $E_k = \eta_{ablator}\eta_{hohlraum}\eta_{laser}E_{laser}$, where η_{laser} is the efficiency of conversion of laser energy to Planckian X-ray energy, $\eta_{hohlraum}$ is the absorption efficiency of hohlraum X-rays by the ablator, and $\eta_{ablator}$ is the efficiency of converting absorbed energy into kinetic energy (generally $\eta_{ablator}\eta_{hohlraum}\eta_{laser} \sim 0.01$). Thus, for the highest yielding high-foot experiments on NIF (shots N140120, N140304, N140511 and N140520), the energy scaling of fusion yields is consistent with being dominated by alpha-particle self-heating.

Although achieving an alpha-heating dominated state is a milestone in inertial confined fusion, the primary purpose of the high-foot pulse-shape implosion has been to create a robust, yet ignition relevant, implosion that behaves systematically as various input parameters are varied. The high-foot implosion thus serves as a way to diagnose trends in implosion behaviour as the very complex parameter space of different drive and capsule conditions is probed. We have studied the response to increasing laser energy (shots N130812–N131119); the effect of implosion shape improvement by changing hohlraum materials from gold to uranium (N131119 versus N140120)[4]; and the apparently null effect of increasing laser power at fixed energy (N140120 versus 140304)[4]. We have also performed tests of repeatability (N131219 versus N140225)[5]; as well as tests of ablator thickness with increasing laser drive: 175 μm ablator 'T-1' (N131219, N140225, N140311 and N140520) and 165-μm-thick ablators 'T-1.5' (N140707 and N140819). Some trends, such as increasing fusion performance with increasing implosion kinetic energy[6], fit expectations, whereas others, such as the null result with increasing laser power at fixed energy, contradict expectations.

As the high-foot implosion is used to probe the envelope of performance space some non-ideal behaviours have become apparent—challenges that must be addressed to make further progress and eventually evolve the design of the implosion on the NIF back towards higher compression, fusion gain, and the ignition[14] threshold. Although ablation-front Rayleigh–Taylor instability and 'mix' has been addressed with the high-foot pulse shape and in pulse shapes that are derivative of it, it has been observed that time-dependent low-mode asymmetries exist in the shells of our implosions, and these distortions increase as we push the implosions to higher levels of compression. The lowest-mode asymmetries are driven by a non-uniform X-ray illumination of the capsule by the hohlraum drive, whereas higher mode, but more localized, asymmetries/instabilities can be caused by engineering features such as the 'tent' diaphragm structure that holds the capsule in the centre of the hohlraum. Other engineering features such as the tube used to fill the capsule with DT are also a concern. Laser–plasma interactions that generate hot electrons (the presence of which is measured in our experiments) that preheat the DT fuel are also a potential performance degradation mechanism and may also be responsible for non-symmetric features on the implosion.

In the upcoming year, our programme will turn its attention to testing new hohlraums with increased diameters as compared with the capsule diameter (increased 'case-to-capsule' ratio). Either through changes in hohlraum geometry or lower helium gas fill, these new hohlraums should minimize hot electrons and create a more isotropic X-ray environment around our implosion using our well-characterized implosion as an integrated diagnostic of whether success has been achieved or not. Coupled to these integrated implosion experiments, a dedicated science team will be working to better measure and characterize the hohlraum plasma environment to better constrain simulations. Collaborative teams will continue working towards assessing the efficacy and trade-offs of alternative ablator materials as well as further maximizing instability control.

Methods

Methods and any associated references are available in the online version of the paper.

Received 8 April 2015; accepted 5 March 2016;
published online 11 April 2016

References

1. Nuckolls, J. *et al*. Laser compression of matter to super-high densities: thermonuclear (CTR) applications. *Nature* **239,** 139–142 (1972).
2. Lindl, J. D. *et al*. The physics basis for ignition using indirect-drive targets on the National Ignition Facility. *Phys. Plasmas* **11,** 339–491 (2003).
3. Hurricane, O. A. *et al*. Fuel gain exceeding unity in an inertially confined fusion implosion. *Nature* **506,** 343–348 (2014).
4. Döppner, T. *et al*. Demonstration of improved performance of fully-integrated deuterium–tritium capsule implosion in depleted uranium hohlraum on the NIF. *Phys. Rev. Lett.* **115,** 055001 (2015).
5. Ma, T. *et al*. Thin-shell high-velocity ICF implosions on the National Ignition Facility. *Phys. Rev. Lett.* **114,** 145004 (2015).
6. Callahan, D. *et al*. Higher velocity high-foot implosions on the National Ignition Facility. *Phys. Plasmas* **22,** 056314 (2015).
7. Kozioziemski, B. J. *et al*. Deuterium–tritium layer formation for the National Ignition Facility. *Fusion Sci. Tech.* **59,** 14–25 (2011).
8. Atzeni, S. & Meyer-ter-Vehn, J. *The Physics of Inertial Fusion* (Oxford Univ. Press, 2004).
9. Spitzer, L. & Harm, R. Transport phenomena in a completely ionized gas. *Phys. Rev.* **89,** 977–981 (1953).
10. Lyon, S. P. & Johnson, J. D. *Sesame: The Los Alamos National Laboratory Equation of State Database* LA-UR-92-3407 (Los Alamos National Laboratory, 1995).
11. Krokhin, O. N. & Rozanov, V. B. Escape of α-particles from a laser-pulse-initiated thermonuclear reaction. *Sov. J. Quant. Electron.* **2,** 393–394 (1973).
12. Town, R. P. J. *et al*. Dynamic symmetry of indirectly driven I. C. F. capsules on the National Ignition Facility. *Phys. Plasmas* **21,** 056313 (2014).
13. Kritcher, A. L. *et al*. Metrics for long wavelength asymmetries in inertial confinement fusion implosions on the National Ignition Facility. *Phys. Plasmas* **21,** 042708 (2014).
14. Lawson, J. D. Some criteria for a power producing thermonuclear reactor. *Proc. Phys. Soc.* **70,** 6–10 (1957).
15. Gus'kov, S. Y., Krokhin, O. N. & Rozanov, V. B. Similarity solution of a thermonuclear burn wave with electron and α-conductivities. *Nucl. Fusion* **16,** 957–962 (1976).
16. Atzeni, S. & Caruso, A. Inertial confinement fusion: ignition of isobarically compressed D-T targets. *Nuovo Cimento B* **80,** 71–103 (1984).
17. Betti, R. *et al*. Deceleration phase of inertial confinement fusion implosions. *Phys. Plasmas* **9,** 2277–2286 (2002).
18. Chang, P. Y. *et al*. Generalized measurable ignition criterion for inertial confinement fusion. *Phys. Rev. Lett.* **104,** 135002 (2010).
19. Yeamans, C. *et al*. Enhanced NIF neutron activation diagnostics. *Rev. Sci. Instrum.* **83,** 10D315 (2012).
20. Park, H.-S. *et al*. High-adiabat, high-foot, inertial confinement fusion implosion experiments on the National Ignition Facility. *Phys. Rev. Lett.* **112,** 055001 (2014).
21. Hurricane, O. A. *et al*. The high-foot implosion campaign on the National Ignition Facility. *Phys. Plasmas* **21,** 056314 (2014).
22. Volegov, P. *et al*. Neutron source reconstruction from pinhole imaging at the National Ignition Facility. *Rev. Sci. Instrum.* **85,** 023508 (2014).
23. Patel, P. *et al*. *Bull. Am. Phys. Soc. 55th Annu. Meeting APS Div. Plasma Phys.* Vol. 58, 16 (American Physical Society, 2013); http://meetings.aps.org/link/BAPS.2013.DPP.NO4.1
24. Cerjan, C., Springer, P. T. & Sepke, S. M. Integrated diagnostic analysis of inertial confinement fusion capsule performance. *Phys. Plasmas* **20,** 056319 (2013).
25. Bleuel, D. L. *et al*. Neutron activiation diagnostics at the National Ignition Facility. *Rev. Sci. Instrum.* **83,** 10D313 (2012).
26. Gatu Johnson, M. *et al*. Neutron spectrometry—an essential tool for diagnosing implosions at the National Ignition Facility. *Rev. Sci. Instrum.* **83,** 10D308 (2012).

27. Glenn, S. *et al*. A hardened gated X-ray imaging diagnostic for inertial confinement fusion experiments at the National Ignition Facility. *Rev. Sci. Instrum.* **81,** 10E539 (2010).
28. Ma, T. *et al*. Imaging of high-energy X-ray emissions from cryogenic thermonuclear fuel implosions on the NIF. *Rev. Sci. Instrum.* **83,** 10E115 (2012).
29. Merrill, F. E. *et al*. The neutron imaging diagnostic at NIF. *Rev. Sci. Instrum.* **83,** 10D317 (2012).
30. Grim, G. P. *et al*. Nuclear imaging of the fuel assembly in ignition experiments. *Phys. Plasmas* **20,** 056320 (2013).
31. Glebov, V. Yu *et al*. Development of nuclear diagnostics for the National Ignition Facility. *Rev. Sci. Instrum.* **77,** 10E715 (2006).
32. Brysk, H. Fusion neutron energies and spectra. *Plasma Phys.* **15,** 611–617 (1973).
33. Frenje, J. A. *et al*. Diagnosing implosion performance at the National Ignition Facility (NIF) by means of neutron spectrometry. *Nucl. Fusion* **53,** 043014 (2013).
34. Murphy, T. J. The effect of turbulent kinetic energy on inferred ion temperature from neutron spectra. *Phys. Plasmas* **21,** 072701 (2014).
35. Spears, B. K. *et al*. *Bull. Am. Phys. Soc. 54th Annu. Meeting APS Div. Plasma Phys.* Vol. 57**,** 12 (American Physical Society, 2012); http://meetings.aps.org/link/BAPS.2012.DPP.GO4.5
36. Betti, R. *et al*. Thermonuclear ignition in inertial confinement fusion and comparison with magnetic confinement. *Phys. Plasmas* **17,** 058102 (2010).
37. Edwards, M. J. *et al*. Progress towards ignition on the National Ignition Facility. *Phys. Plasmas* **20,** 070501 (2013).
38. Dittrich, T. R. *et al*. Design of a high-foot/high-adiabat ICF capsule for the National Ignition Facility. *Phys. Rev. Lett.* **112,** 055002 (2014).
39. Meezan, N. B. *et al*. Cryogenic THD and DT layer implosions with high density carbon ablators in near-vacuum hohlraums. *Phys. Plasmas* **22,** 062703 (2015).

Acknowledgements

We gratefully acknowledge thoughtful discussions with R. Betti (LLE), D. Clark, J. Hammer, J. Hayes, M. C. Herrmann, W. Hsing, B. Kauffman, J. Kilkenny, R. Kirkwood, B. MacGowan, A. Mackinnon, N. Meezan, J. Nuckolls, L. Peterson, J. Pino, K. Raman, B. A. Remington, M. Rosen, V. Smalyuk, C. Thomas and B. Van Wonterghem. Thanks to the NIF's operations, diagnostics, cryogenics, target, and project engineering teams (B. Burr, P. Kervin, L. Kot, J. Meeker, D. Swift and B. Young). Thanks to external collaborators at LANL (diagnostics), GA (targets), LLE (diagnostics), the MIT Plasma Science and Fusion Center (MRS diagnostic), CEA and AWE. This work was performed under the auspices of the US Department of Energy by Lawrence Livermore National Laboratory under Contract No. DE-AC52-07NA27344.

Author contributions

O.A.H. high-foot (HF) team co-lead dynamic model development and synthesis; D.A.C. HF team co-lead hohlraum drive and symmetry; D.T.C. DT shots (experiments) co-RI (responsible individual); E.L.D. 1DConA (velocity measurement) Shot RI, re-emit (X-ray re-emission experiment) Shot RI and data analysis and hot-electron analysis; T.R.D. 1D design physics and scoping; T.D. DT Shot RI and hard X-ray imaging analysis; S.H. DT ice layer characterization and instability growth-factor calculations; D.E.H. integrated hohlraum–capsule pulse-shape design physics and integrated post-shot modelling; L.F.B.H. keyhole (shock wave timing) shot pulse-shape design and post-shot modelling; O.J. hohlraum model design and development; A.L.K. integrated post-shot modelling and asymmetry analysis; S.L. keyhole Shot RI; T.M. DT Shot RI and hotspot shape analysis; A.G.M. capsule X-ray yield, data analysis tools, and 1DConA co-RI; J.L.M. hohlraum model development and re-emit design; J.M. hohlraum and backscatter physics experiments; A.P. DT Shot co-RI, re-emit Shot RI and analysis, and hotspot shape analysis; H.-S.P. DT Shot RI; P.K.P. post-shot data analysis and hotspot model energy, pressure, and alpha-heating analysis; J.E.R. Symcap (hotspot symmetry measurement) Shot RI and backscatter analysis; H.F.R. keyhole platform design and hot-electron studies; J.S.R. hohlraum experiments; J.D.S. 1D post-shot modelling; B.K.S. development model database for alpha-heating analysis and NToF data analysis; P.T.S. hotspot, dynamic model development, and fit of Q_{cond} to SESAME database; R.T. 1DConA shot co-RI, data analysis and unfold of 2DConA data; F.A. FFLEX (hot-electron) data analysis; L.R.B. time-resolved hotspot shape X-ray measurement; R.B. FNADS (nuclear activation) spatial analysis; E.B. NToF data analysis; D.K.B. 2DConA (ablator shape) platform development; J.C. NToF data analysis; P.M.C. keyhole VISAR data analysis; C.C. 3D hotspot model analysis; J.A.C. GRH (gamma reaction history); R.D.S. DT ice layer cryogenics; D.E. south-pole bang-time data analysis; M.J.E. Program Director; D.F. NIS (neutron imaging system) LLNL RS (responsible scientist); M.A.B.G. 2DConA Shot RI; A.H. target fabrication engineering; R.H. NToF data analysis; H.H. GRH data analysis; M.H. FFLEX data synthesis; D.H. target engineering; J.L.K. Symcap Shot RI and Dante (low-resolution X-ray temperature measurement) analysis; B.K. DT ice layer cryogenics and cryo-team science lead; G.K. X-ray imaging and analysis; G.G. fields and performs data analysis for the neutron imaging time-of-flight system; J.E.F. 2DConA data analysis; J.F. MRS (magnetic recoil spectrometer) diagnostic analysis; N.I. X-ray image data analysis; M.G.J. MRS diagnostic analysis; S.F.K. X-ray image analysis; J.K. nuclear data analysis; T.K. DT fuelling and tritium facility lead; O.L. fuel velocity inference; F.M. NIS LANL RS and performs data reduction, analysis, and error determination; P.M. hohlraum cross-bean energy transfer model and analysis; A.M. Dante diagnostic RS; S.R.N. 2DConA Shot co-RI, DIXI X-ray data analysis; A.N. target fabrication engineering; T.P. cryogenics and DT fuel team; R.R.R. 2DConA data analysis; D.S. GRH; M.S. soft X-ray imaging analysis; D.S. spectral radio-chemistry data analysis; D.S. backscatter analysis; R.P.J.T. 2DConA platform design; A.W. high energy density program lead; K.W. Dante diagnostic RS; C.W. NIS diagnostic RI; P.V. develops algorithms to extract source information from NIS coded aperture; C.Y. FNADS (flange nuclear activation diagnostic system) analysis.

Additional information

Reprints and permissions information is available online at www.nature.com/reprints. Correspondence and requests for materials should be addressed to O.A.H.

Competing financial interests

The authors declare no competing financial interests.

Methods

Justification for the acceptability of the optically thin limit of the bremsstrahlung X-ray cooling power is given. The scaling with temperature of the fusion reaction rate over different temperature regimes is shown. A partial set of analytic solutions to the dynamic model equations of this paper is given in the limit of balanced alpha-heating and X-ray losses.

Radiation losses: optical thin limit versus line radiation model. In Fig. 4, the X-ray energy radiated from the hotspot using the measured temperature, volume and inferred density for a variety of NIF implosions is compared under two different assumptions: using a detailed 1D transport model with a radial density profile and detailed configuration accounting opacities (ordinate) and the expression for bremsstrahlung losses in the optically thin limit, Q_{Brems} of the text (abscissa).

DT fusion reaction-rate scalings. Useful power-law, in temperature (T), approximations to the DT reaction rate (in $\mathrm{cm}^3\ \mathrm{s}^{-1}$; ref. 40) are:

$$\langle\sigma v\rangle = 1.66\times10^{-20}T^{4.3}\pm9\%,\ 2\le T\le4 \tag{7}$$

$$\langle\sigma v\rangle = 2.68\times10^{-20}T^{3.9}\pm13\%,\ 3\le T\le5 \tag{8}$$

$$\langle\sigma v\rangle = 4.15\times10^{-20}T^{3.6}\pm3\%,\ 4\le T\le6 \tag{9}$$

$$\langle\sigma v\rangle = 1.48\times10^{-19}T^{2.9}\pm5\%,\ 6\le T\le9 \tag{10}$$

Hotspot dynamic equations in the adiabatic implosion limit. With P_0 and R_0 being the hotspot pressure and radius at peak velocity, v_0, at $t=0$, the adiabatic compression condition ($P_{\mathrm{hs}}R^5\approx P_0R_0^5=$const. when the right-hand side of equation (6) is negligible) allows a simple solution to equation (1). Namely,

$$R(t)=\sqrt{R_{\mathrm{min}}^2+\frac{4\pi P_0R_0^5}{\epsilon m_{\mathrm{shell}}R_{\mathrm{min}}^2}(t-t_{\mathrm{min}})^2} \tag{11}$$

$$\dot{R}(t)=\mp\sqrt{\frac{4\pi P_0R_0^5}{\epsilon m_{\mathrm{shell}}}\left(\frac{1}{R_{\mathrm{min}}^2}-\frac{1}{R^2}\right)} \tag{12}$$

$$R_{\mathrm{min}}=\frac{R_0}{\sqrt{1+\frac{\epsilon m_{\mathrm{shell}}v_0^2}{4\pi P_0R_0^3}}}\approx R_0\sqrt{\frac{4\pi P_0R_0^3}{\epsilon m_{\mathrm{shell}}v_0^2}}\sim E_{\mathrm{k}}^{-1/2} \tag{13}$$

$$t_{\mathrm{min}}=\frac{v_0R_0}{v_0^2+\frac{4\pi P_0R_0^3}{\epsilon m_{\mathrm{shell}}}}\approx R_0/v_0 \tag{14}$$

where R_{min} is the minimum implosion radius and t_{min} is the time between peak velocity and minimum radius. We are generally interested in the case where the kinetic energy of the shell at peak velocity considerably exceeds the hotspot internal energy, $2\pi P_0R_0^3$, hence the approximate solutions above. The importance of the ratio of shell kinetic energy to hotspot internal energy has been noted previously[17]. We note the peak stagnation pressure is achieved at R_{min}, so $P_{\mathrm{stag}}=P_0(R_0/R_{\mathrm{min}})^5\sim E_{\mathrm{k}}^{5/2}$. In the ion temperature range of 3–5 keV, the fusion yield then scales as $Y\sim P_{\mathrm{stag}}^2T^{1.9}V_{\mathrm{hs}}\tau_{\mathrm{burn}}\sim E_{\mathrm{k}}^5T^{1.9}V_{\mathrm{hs}}\tau_{\mathrm{burn}}$, where τ_{burn} is the burn duration of the implosion. In equation (5) if one drops the bremsstrahlung and mass loss terms, and then approximates $\mathrm{d}T/\mathrm{d}t\sim-Tv_0/R_{\mathrm{min}}$, the relation $T\sim E_{\mathrm{k}}^{1/2}v_0^{1/3}$ similar to ref. 18 is obtained. Thus, with no alpha-heating and no energy losses, the fusion yield will scale as $Y\sim E_{\mathrm{k}}^{4.0}/v_0^{0.63}$, because $V_{\mathrm{hs}}\tau_{\mathrm{burn}}\sim R_{\mathrm{min}}^4/v_0$.

References

40. Bosch, H. S. & Hale, G. M. Improved formulas for fusion cross-section and thermal reactivities. *Nucl. Fusion* **32,** 611–631 (1992).